Synthetic observations of protostellar multiple systems

O. Lomax★ and A. P. Whitworth
School of Physics and Astronomy, Cardiff University, Cardiff CF24 3AA, UK

ABSTRACT

Observations of protostars are often compared with synthetic observations of models in order to infer the underlying physical properties of the protostars. The majority of these models have a single protostar, attended by a disc and an envelope. However, observational and numerical evidence suggests that a large fraction of protostars form as multiple systems. This means that fitting models of single protostars to observations may be inappropriate. We produce synthetic observations of protostellar multiple systems undergoing realistic, non-continuous accretion. These systems consist of multiple protostars with episodic luminosities, embedded self-consistently in discs and envelopes. We model the gas dynamics of these systems using smoothed particle hydrodynamics and we generate synthetic observations by post-processing the snapshots using the SPAMCART Monte Carlo radiative transfer code. We present simulation results of three model protostellar multiple systems. For each of these, we generate 4×10^4 synthetic spectra at different points in time and from different viewing angles. We propose a Bayesian method, using similar calculations to those presented here, but in greater numbers, to infer the physical properties of protostellar multiple systems from observations.

Key words: hydrodynamics – radiative transfer – methods: numerical – binaries: close – dust, extinction.

1 INTRODUCTION

Stars form when dense prestellar cores in molecular clouds collapse under their own self-gravity. These cores are turbulent (e.g. André et al. 2007) and therefore have net angular momentum. From conservation of angular momentum, any protostar which forms during the initial core collapse is likely to be attended by a circumstellar disc. As the remainder of the core envelope collapses inwards, additional material accretes on to the disc. Dissipative phenomena such as viscosity (e.g. Stamatellos & Whitworth 2008) and magnetic braking (e.g. Zhu et al. 2007) transport angular momentum to the outer the regions of the disc, allowing material in the inner regions to accrete on to the protostar.

Further protostars may form via disc fragmentation if the following two criteria are met. First, the surface density of the disc must be great enough for self-gravity to overcome thermal and centrifugal support (Toomre 1964). Secondly, the cooling time of a potential fragment must be shorter than its orbital period (Gammie 2001). The time-scale on which disc fragmentation occurs is very short ($t_{\mathrm{FRAG}} \sim 10^4$ yr; e.g. Stamatellos & Whitworth 2008), which makes observing the process difficult. However, observations of young protostellar multiples show separations consistent with disc fragmentation (e.g. Tobin et al. 2016). Furthermore, numerical simulations of disc fragmentation are able to reproduce the mass distribution and multiplicity statistics of low-mass stars and brown dwarfs (e.g. Stamatellos & Whitworth 2009; Lomax et al. 2014, 2015; Lomax, Whitworth & Hubber 2015).

Accretion luminosity is the dominant source of radiative feedback for young protostars. Calculations that include continuous radiative feedback from accretion on to protostars produce discs, which are too hot to fragment (e.g. Bate 2009; Krumholz 2006; Krumholz et al. 2010; Offner et al. 2009, 2010). This supports the hypothesis that disc fragmentation does not occur often. However, this hypothesis is weakened by the observed luminosities of young protostars. These are much lower than those predicted by continuous accretion models. This is known as the *luminosity problem* (first noted by Kenyon et al. 1990). This problem is alleviated by observational evidence suggesting that protostellar luminosities are episodic. For example, FU Ori stars exhibit luminosity outbursts, which last of order decades (e.g. Hartmann & Kenyon 1996; Greene, Aspin & Reipurth 2008; Peneva et al. 2010). Similarly, knots have been observed in protostellar outflows, which have spacings suggestive of episodic accretion (e.g. Reipurth 1989). Simulations which include sub-grid models of episodic accretion demonstrate that significant disc fragmentation may still occur if radiative feedback is episodic (e.g. Stamatellos, Whitworth & Hubber 2011, 2012).

Inferring the physical properties of young protostars requires matching their observables, for example, their spectral energy distributions (SEDs), with those of models. Great efforts have been made to construct large catalogues of SEDs from model protostars with realistic dust properties and varied protostar and disc

★ E-mail: oliver.lomax@astro.cf.ac.uk

parameters (e.g. Robitaille et al. 2006). Additionally, previous work has modelled the observable features of embedded stars with variable luminosity (e.g. Harries 2011; Johnstone et al. 2013). However, in all these cases the stars are single, and there is growing observational and theoretical evidence that a large fraction of stars form as multiples (e.g. Kraus et al. 2011; Holman et al. 2013; Bate 2014; Lomax et al. 2015). Here, we simulate the observational signatures of embedded protostellar multiple systems via a two-stage process. First, we use smoothed particle hydrodynamics (SPH) to simulate the collapse and fragmentation of turbulent prestellar cores. This uses an approximate on-the-fly radiative transfer method and sink particles that have episodic luminosities determined by a subgrid model involving the magneto-rotational instability (Balbus & Hawley 1991). Secondly, we post-process snapshots from the simulations using a Monte Carlo radiative transfer algorithm to calculate the dust emission and scattered light.

In Section 2, we detail the numerical methods used to perform the calculations. In Section 3, we describe the initial conditions and results of the SPH simulations. In Section 4, we define the parameters of the radiative transfer calculations and describe their results. In Section 5 ,we discuss the significance of these calculations, and propose a methodology for using them to interpret the properties of protostars from observations. Finally, we summarize our findings in Section 6.

2 NUMERICAL METHOD

In this section, we outline the numerics of this work. Some of the more technical issues are included as appendices. If the reader is unconcerned with these details, we suggest they skip to Section 3.

2.1 Smoothed particle hydrodynamics

Core evolution is simulated using the SEREN ∇h-SPH code (Hubber et al. 2011), with $\eta = 1.2$ and the Morris & Monaghan (1997) formulation of time dependent artificial viscosity. SPH particles have mass $m_{SPH} = 10^{-5} \, M_{\odot}$, and the minimum mass for star formation ($\sim 3 \times 10^{-3} \, M_{\odot}$; see Whitworth & Stamatellos 2006) is resolved with ~ 300 particles. Gravitationally bound regions with densities higher than $\rho_{SINK} = 10^{-9} \, g \, cm^{-3}$ are replaced with sink particles. These use the NEWSINKS smooth accretion algorithm (Hubber, Walch & Whitworth 2013). Sink particles have radius $r_{SINK} \simeq 0.2$ au, corresponding to the smoothing length of an SPH particle with density equal to ρ_{SINK}. The equation of state and the energy equation are treated with the radiative transfer approximation described by Stamatellos et al. (2007; hereafter SW07).

Episodic radiative feedback from sinks is also included. Each sink has a variable luminosity, which follows the sub-grid episodic accretion model described in Stamatellos et al. (2011; hereafter SWH11). Here, the mass of a sink is split into its stellar mass $M_{\star}$ and a mass attributed to an unresolved inner accretion disc (IAD) M_{IAD}. The total mass $M = M_{\star} + M_{IAD}$ is used for all gravitational force calculations in the simulations. Mass that accretes on to the sink is added to M_{IAD}. This mass is then transferred from the IAD to the star via a low quiescent accretion phase, which is punctuated by intense episodic outbursts. These outbursts almost completely deplete the mass of the IAD. The mass transfer rate from the IAD to the star is used to calculate the luminosity of a sink particle. The parameters of this model (e.g. episode intervals and duration) are based on calculations involving the magneto-rotational instability by Zhu, Hartmann & Gammie (2009, 2010) and Zhu et al. (2010). This produces sinks with low accretion luminosities, which briefly

increase by a couple of orders of magnitude every $\sim 10^4$ yr. The duration of each outburst is $\sim 2 \times 10^2$ yr.

2.2 Post-processing radiative transfer

2.2.1 Smoothed particle Monte Carlo radiative transfer

We perform post-process dust radiative transfer calculations on simulation snapshots using the SPAMCART Monte Carlo code (Lomax & Whitworth 2016, hereafter LW16). The algorithm is a gridless adaptation of the Lucy (1999) method, designed to operate on smoothed particles instead of uniform density cells. Here, the gas particles from the simulation represent the dusty interstellar medium. The sink particles are treated as isotropic point sources with luminosities $L_{\star}$ given by the SWH11 model.[1] We assume each sink has a black-body SED determined by $L_{\star}$ and an assumed radius $R_{\star} = 3 \, M_{\odot}$. In addition, we include the local interstellar radiation field calculated by Porter et al. (2008). The sources emit luminosity packets, which propagate through the SPH density field until they escape the system. The dust properties of the particles are defined and discussed in Appendix A1.

The energy absorbed, per unit time, per unit mass of dust, for a particle is estimated by summing the optical depth contributions from luminosity packets, which pass through the particle's smoothing kernel,

$$\dot{A}_i \simeq \frac{\ell_j}{m_i} \sum_j \kappa_{\lambda_j} \, \varsigma_{ij}. \tag{1}$$

Here, ℓ_j is the luminosity attributed to packet j, λ_j is its wavelength, m_i is the dust mass of particle i, ς_{ij} is the column density along the trajectory of packet j through particle i, and κ_{λ_j} is the dust absorption opacity at λ_j.

The energy scattered, per unit time, per unit mass, per unit wavelength can be estimated by summing packets with λ_j in the interval $[\lambda, \lambda + d\lambda]$. Here,

$$\dot{S}_{i\lambda} \, d\lambda \simeq \frac{\ell_j}{m_i} \sum_{j, d\lambda} \sigma_{\lambda_j} \, \varsigma_{ij}, \tag{2}$$

where σ_{λ_j} is the dust scattering opacity at λ_j. Note that we assume dust scattering is isotropic. Additional features of the code, such as dust sublimation and dealing with very high opacities, are discussed in Appendices A2 and A3.

We generate synthetic images and spectra of dust emission and scattered light by performing a ray trace for each pixel of a virtual camera. We identify the collection of particles which are intersected by a ray centred on and normal to the pixel. They are then sorted is descending order of distance from the pixel. The intensity (or surface brightness) $I_{\lambda n}$ at the pixel position is calculated iteratively from $i = 1$ to n, where

$$I_{\lambda i} = I_{\lambda i-1} \exp(-\chi_{\lambda} \, \varsigma_i) + j_{\lambda i} \, [1 - \exp(-\chi_{\lambda} \, \varsigma_i)]. \tag{3}$$

Here, $I_{\lambda 0}$ is the intensity of the background interstellar radiation field, $\chi_{\lambda} \equiv \kappa_{\lambda} + \sigma_{\lambda}$ is the dust mass extinction at λ, and ς_i is the column density along the ray through particle i. The source function

---

[1] We note that the assumption of isotropy is a simplification. In nature, the protostars have IADs, which focus emergent radiation towards the protostellar poles. This anisotropy is further increased by the presence of protostellar jets, which are not modelled here. We comment on this further in Section 5.2.

$j_{\lambda i}$ is given by

$$j_{\lambda i} = \frac{1}{\chi_\lambda} \left[B_\lambda(T_i)\kappa_\lambda + \frac{\dot{S}_{\lambda i}}{4\pi} \right], \tag{4}$$

where $B_\lambda(T)$ is the *Planck* function and T_i is found by inverting the equation

$$\dot{A}_i = 4\,\sigma_{\text{SB}}\,\bar{\kappa}_{\text{P}}(T_i)\,T_i^4. \tag{5}$$

Here, σ_{SB} is the Stefan–Boltzmann constant and $\bar{\kappa}_{\text{P}}(T)$ is the Planck mean mass absorption coefficient. Images are constructed using a quadtree of rays. We adaptively refine the image plane until *every* particle has *at least* one ray with an impact parameter shorter than its smoothing length. In most cases, the intensity maps refine down to length scales $\lesssim 0.1$ au, which allows us to resolve the sublimation radii of most protostars. We note that these intensity maps can display visible pixelation in low-intensity regions. This is a necessary trade-off; if the maximum resolution was applied over the entire area, most of the maps presented here would be made up of roughly 10^9 pixels. Storing and processing this large a quantity of data is impractical, given that we want to generate a large number of multi-wavelength data cubes. Direct starlight from sink particles, attenuated by dust, is added to the image after calculating the dust emission and scattered light.

2.3 Code benchmark

Performing benchmarks for radiative transfer codes is often difficult. In most cases, multiple codes must be tested against each other in a labour-intensive study (e.g. Bisbas et al. 2015; Gordon et al. 2017). We acknowledge that this should be examined in future work. Here, instead, we perform a benchmark that demonstrates the code's ability to reproduce Kirchoff's law of thermal radiation. This benchmark is discussed in detail in Appendex B. We show that when an object (in this case, a non-spherically symmetric distribution of particles) reaches thermal equilibrium with a blackbody radiation field, the object is indistinguishable from the background. This applies for all viewing directions. When the background radiation field is that of a diluted blackbody, the object casts a silhouette against the background at short wavelengths, and glows relative to the background at long wavelengths.

3 SPH SIMULATIONS

3.1 Initial conditions

We run three simulations of prestellar cores, one with the initial conditions taken from Lomax et al. (2015), and two chosen from the ensemble generated by Lomax et al. (2014). We apply a turbulent velocity field with a thermal mix of solenoidal to compressive modes and a $P(k) \propto k^{-4}$ power spectrum. The core density profile is that of a critical Bonner–Ebert sphere.[2] The masses, sizes, and non-thermal velocity dispersions of the cores are given in Table 1. The core parameters are chosen because (i) they are similar to some of the observed cores in Ophiuchus, (ii) the masses roughly span the dynamic range observed in nearby young star-forming regions, and (iii) previous simulations, similar to these, produce more than one embedded protostar. We note that the setups are cherry-picked for their high multiplicities and the results should not be

---

[2] We simply use the density profile of a critical Bonner–Ebert sphere. The cores are neither isothermal, nor in hydrostatic equilibrium.

Table 1. Core masses, M_{CORE}, radii, R_{CORE}, and non-thermal velocity dispersions, σ_{NT}. The parameters of Core A are taken from Lomax et al. (2015). Cores B and C are chosen from the ensemble generated by Lomax et al. (2014).

Core	M_{CORE} (M$_\odot$)	R_{CORE} (au)	σ_{NT} (km s^{-1})
A	2.9	3100	0.44
B	1.0	3200	0.10
C	0.5	2400	0.22

Table 2. The number of protostars, $N_\star$, and their masses, $M_\star$, formed in each core simulation.

Core	$N_\star$	$M_\star$ [M$_\odot$]
A	5	0.68, 0.56, 0.54, 0.44, 0.02
B	7	0.44, 0.09, 0.07, 0.06, 0.05, 0.01, 0.01
C	4	0.04, 0.03, 0.02, 0.02

used to make statistical arguments. The simulations are terminated at $t = 2 \times 10^5$ yr, by which point accretion on to the protostars has ceased. This corresponds to the crossing time of cores in Ophiuchus, estimated by André et al. (2007).

3.2 Results

Here, we provide a brief overview of the evolution of each core. The number of protostars formed in each core simulation, along with their masses, is given in Table 2. Intensity maps and SEDs highlighting the evolution Cores A, B, and C are given in Figs 1, 2, and 3, respectively.

3.2.1 Core A

Due to the strong turbulent velocity field, Core A fragments simultaneously into three protostars at $t \approx 1.0 \times 10^4$ yr. These quickly assemble into a triple system, attended by a circumsystem accretion disc. A fourth protostar forms via a gravitational instability in one of the accretion flows on to the disc at $t \approx 1.5 \times 10^4$ yr. The protostar quickly merges with the triple system to form a twin binary quadruple system. Additionally, gravitationally unstable material within the circumsystem disc fragments into a fifth object at $t \approx 1.7 \times 10^4$ yr. This object accretes very little mass and is ejected from the system at $t \approx 3.0 \times 10^4$ yr. The final system configuration is a twin binary quadruple system, composed of four proto-K-dwarfs, and an ejected proto-brown dwarf. By $t = 2 \times 10^5$ yr, 75 per cent of the original core mass has accreted on to the protostars.

3.2.2 Core B

Core B collapses into a single protostar at $t \approx 3.0 \times 10^4$ yr. A second protostar forms via disc fragmentation at $t \approx 5.0 \times 10^4$ yr, producing a binary system with a circumbinary disc. At $t \approx 6.0 \times 10^4$ yr, the disc fragments into a further five protostars. Two of these merge with the binary to form a twin binary quadruple of brown dwarfs. Later in the simulation, the other three objects are ejected as a single brown dwarf and a binary pair of brown dwarfs. By $t \approx 2 \times 10^5$ yr, 70 per cent of the original core mass has accreted on to the protostars.
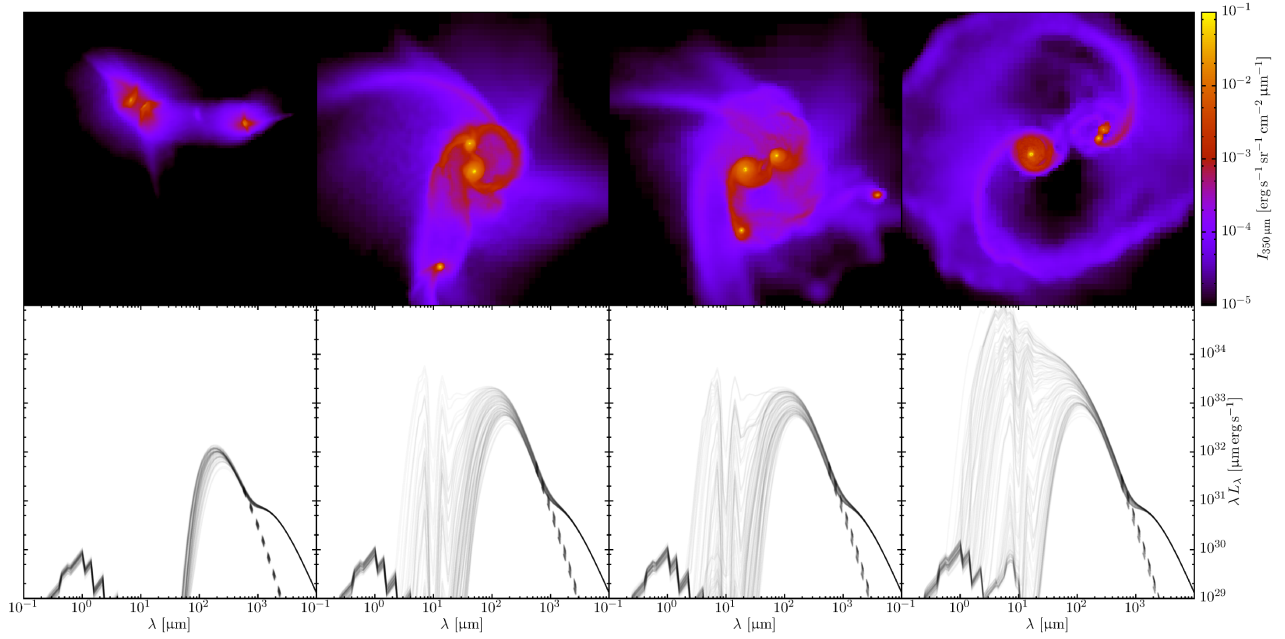
Figure 1. Synthetic observations of Core A. From the left- to right-hand side, the columns show snapshots at $t = 1.0, 1.5, 1.7$, and 3.0×10^4 yr. The top row shows the unconvolved 350 μm intensity integrated along a fixed line of sight. The edge-length of each frame is 1300 au. The bottom row shows an ensemble of source SEDs, seen through one hundred randomly chosen lines of sight. The solid lines show the full SEDs and the dashed segments show the SEDs after the CMB has been subtracted. The short wavelength component of the SEDs ($0.3 \lesssim \lambda \lesssim 3\,\mu$m) is predominantly scattered light from the interstellar radiation field.
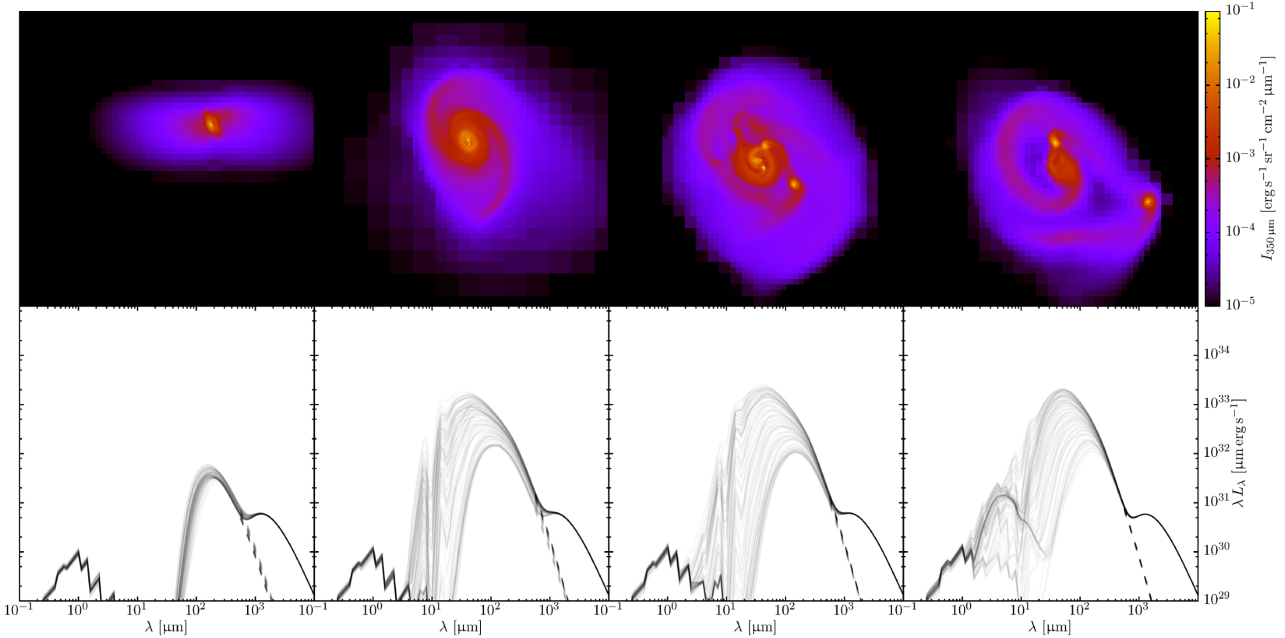
Figure 2. As Fig. 1, but for Core B at $t = 2.0, 4.0, 5.0$, and 6.5×10^4 yr. The edge length of each map is 700 au.

3.2.3 Core C

Core C collapses into a single a protostar at $t \approx 2.0 \times 10^4$ yr. Three more protostars form via disc fragmentation between $t \approx 2.2$ and $t \approx 2.3 \times 10^4$ yr. The protostars settle into a twin binary quadruple (four brown dwarfs) by $t \approx 3.0 \times 10^4$ yr. By $t \approx 2 \times 10^5$ yr, 25 per cent of the original core mass has accreted on to the protostars.

4 POST-PROCESSING RADIATIVE TRANSFER

4.1 Calculation parameters

For each core, we post-process 400 snapshots linearly spaced in time with an interval of 100 yr. The ranges of these time series are shown by the x-axes in Fig. 4. Each time series is limited to 4×10^4 yr in order to reduce computational expense.
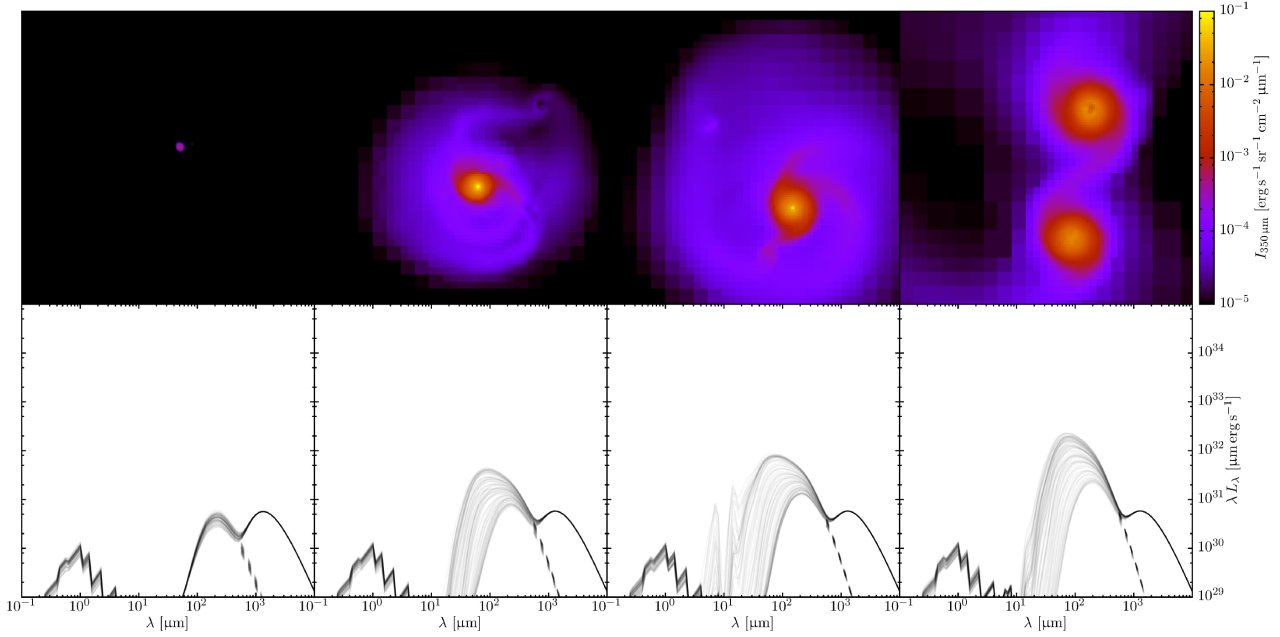
Figure 3. As Fig. 1, but for Core C at $t = 1.7, 2.2, 2.3$, and 3.0×10^4 yr. The edge length of each map is 300 au.
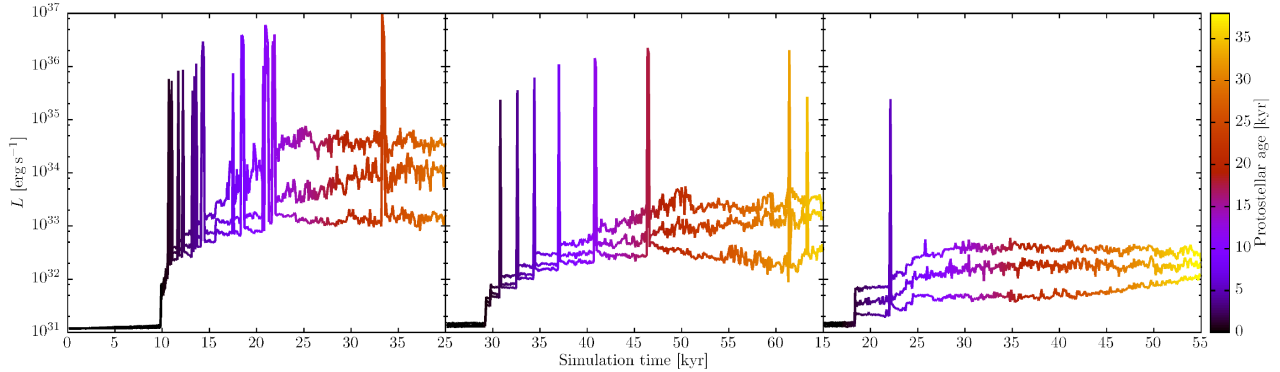
Figure 4. Apparent luminosities of Core A, Core B, and Core C (for the left- to right-hand side) as a function of simulation time. The three lines show the 15th, 50th, and 85th centile values, seen through one hundred randomly chosen lines of sight. The colour scale shows the protostellar age, i.e. the age of the system where $t = 0$ marks the formation of the first sink particle.

For each of these calculations we inject 10^6 equal-luminosity packets into the system from point sources, and 10^6 luminosity packets into the system from the external radiation field. We iterate the calculation five times, after which the total luminosity from dust, i.e. $\sum_i A_i m_i$ for all particles, has converged to within a few percent.

For each post-processing calculation, we generate intensity maps from 100 random viewing directions, at 100 wavelengths equally spaced logarithmically in the range $10^{-1}\,\mu\text{m} \leq \lambda \leq 10^4\,\mu\text{m}$. Each intensity map covers a 1500 au square centred on the particle ensemble's centre of mass. We generate SEDs for each line of sight by integrating over the image plane at each wavelength.

4.2 Results

4.2.1 Photometry

Fig. 4 shows the apparent luminosity of Core A, Core B, and Core C as a function of time, where

$$L = \int_0^\infty L_\lambda \, d\lambda \, ;$$

$$L_\lambda = 4\pi \int_A I_\lambda \, dA. \tag{6}$$

Here, A is the surface area of the map, which is equivalent to the solid angle subtended on the sky, multiplied by the distance to the source squared. Note that L varies with viewing angle unless the source is isotropic or completely optically thin. The three lines in each plot of Fig. 4 show the 15th, 50th, and 85th centile values of L from multiple viewing angles as a function of time. The large peaks every $\sim 10^4$ yr show the episodic outburst events. In general, these are much more frequent from more massive protostars. Between accretion bursts, the apparent luminosity depends strongly on viewing angle. The sources can easily appear 3–10 times more or less luminous than they really are. During an outburst, the variation with viewing angle is greatly reduced. This is because the increased stellar luminosity
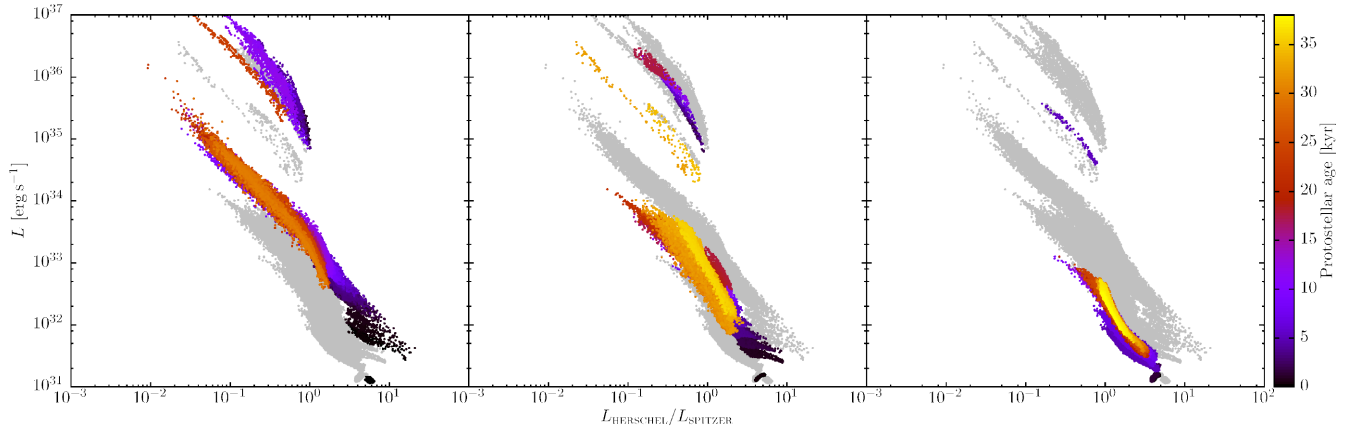
Figure 5. Apparent luminosities of Core A, Core B, and Core C (from the left- to right-hand side) plotted against infrared colour. Here, we define colour as the amount of luminosity in a *Herschel*-like band ($55 \leq \lambda \leq 672 \, \mu$m) over that in a *Spitzer*-like band ($3 \leq \lambda \leq 180 \, \mu$m). In each plot, the coloured points show the data related to the specific core. Data for the remaining two cores are shown in grey to provide a comparison. The colour scale shows the protostellar age and is the same as in Fig. 4 .

clears out a sublimation radius of $\sim$2 au (see Appendix A2) around the star, allowing radiation to escape easily in many directions. We note that in most cases, disentangling the apparent luminosity of each individual star is difficult as the direct stellar radiation is almost entirely reprocessed by the surrounding dust.

The protostars in Core A settle to a median total luminosity[3] of $L \sim 10^{34}$ erg s^{-1}, roughly 3×10^{4} yr after the formation of the first protostar ($L_{\odot} = 3.8 \times 10^{33}$ erg s^{-1}). By this point, the four most massive protostars contribute approximately 40 per cent, 20 per cent, 20 per cent, and 20 per cent of the total system luminosity. Over this time period, twelve episodic outbursts, each lasting $\lesssim 10^{2}$ yr, temporarily raise the system luminosity by three orders of magnitude. The protostars in Core B settle to a median total luminosity of $L \sim 10^{33}$ erg s^{-1} after 3×10^{4} yr. Here, the six most massive stars contribute 70 per cent, 13 per cent, 8 per cent, 4 per cent, 3 per cent, and 2 per cent of the total luminosity. Eight episodic outbursts occur during this period. The protostars in Core C reach a median total luminosity of $L \sim 10^{32}$ erg s^{-1} within 10^{4} yr. Here, the four most massive protostars contribute approximately 40 per cent, 20 per cent, 20 per cent, and 20 per cent of the total luminosity. Only one episodic outburst occurs during this period.

Fig. 5 shows the colour–luminosity diagram for each protostellar system, over all times and viewing angles. Here, we define colour as the amount of luminosity in a *Herschel*-like band ($55 \leq \lambda \leq 672 \, \mu$m) over that in a *Spitzer*-like band ($3 \leq \lambda \leq 180 \, \mu$m). We refer to objects with low values of $L_{\mathrm{HERSCHEL}}/L_{\mathrm{SPITZER}}$ as blue, and those with high values as red.

During the prestellar phase, each core has a low luminosity and is relatively red. As protostars form within the cores, the system move on to a *main track* where they appear more blue and luminous the closer they are to being viewed face on. *Secondary tracks* appear above the main track during episodic outbursts. While all three cores share these features, Core A has a bluer and more luminous main track than Core B, which has a bluer and more luminous main track than Core C.

4.2.2 Spectral features

Figs 1, 2, and 3 show $350 \, \mu$m specific intensity maps and SEDs for Cores A, B, and C, respectively. All of the SEDs display some common features. At wavelengths $10^{3} \leq \lambda \leq 10^{4} \, \mu$m, the radiation is primarily from the cosmic microwave backgrounds (CMB). The radiation at wavelengths $10^{-1} \leq \lambda \leq 10^{1} \, \mu$m is mostly scattered light from the interstellar radiation field.[4] In between these bands, the radiation is predominantly dust emission from the core envelope and/or protostellar discs. This varies strongly from source to source as well as over time and through different viewing angles. We note that in the majority of cases, luminosity packets from protostars undergo 10^{4} to 10^{6} absorption/reemission or scattering events before they escape the system. Therefore the SED shape of the protostellar photosphere makes almost no contribution to the full system SED.

During the prestellar and very early protostellar stages of the simulations, i.e. where a protostar has formed but accounts for $\lesssim 10$ per cent of the total mass, the dust emission from all three cores resembles a [$T \sim 15$ K, $\beta \sim 2$] modified blackbody. Here, the source is only bright at wavelengths $10^{2} \lesssim \lambda \lesssim 10^{3} \, \mu$m. The SED is only weakly dependent on viewing angle because the protostars are still embedded in dense clumps with some degree of spherical symmetry. Short wavelength emission is degraded to longer wavelengths in all directions. As the protostars evolve over the next $\sim 10^{4}$ yr (during which secondary protostars also form via disc fragmentation), they heat nearby dust and become bright at wavelengths $10 \lesssim \lambda \lesssim 10^{2} \, \mu$m. As these systems are roughly coplanar, most of the radiation can only escape at angles close to the rotational axis of the system. Systems with sufficiently luminous embedded protostars also emit significant amounts of radiation at wavelengths $1 \lesssim \lambda \lesssim 10 \, \mu$m. This is seen strongly in Core A and moderately in Core B.

The systems described here are naturally dynamic and their morphologies can change dramatically over the course of $\lesssim 10^{4}$ yr. For example, Core C quickly transitions from an unstable disc around a single protostar to a stable quadruple system. While these events do not necessarily produce an obvious tracer in the SEDs, they

---

[3] Here, the median value is similar to the direction-averaged mean value (i.e. the *true* luminosity) to within a factor of a few. However, unlike the mean, the median is less sensitive to statistical outliers. In most cases, the median is less than the mean value.

[4] Note that the jagged features in the SED are caused by the wavelength binning of scattered luminosity packets during the calculation. This bin size can be reduced at the cost of introducing greater statistical noise.

can occasionally produce some unusual spectra. In Core A (see the last frame of Fig. 1), the final quadruple system forms during an event where a relatively discless protostar destroys the disc of another, forming a binary system. This allows emission from hot dust near the two protostars to escape without being reprocessed by a cool disc. The result of this is a sustained spike in the emission at $\lambda \lesssim 10\,\mu m$. Another peculiar spectrum is observed in Core B (see the last frame of Fig. 2). Here, the system is in a dynamically unstable state and radiation with $\lambda \lesssim 10\,\mu m$ from dust around one of the objects is more easily observed from an edge on viewing angle than it is face on.

4.2.3 Viewing angle case study

Once a disc has formed, the apparent luminosity of the protostars usually varies strongly with viewing angle. Here, we perform a case study by examining the SEDs of a snapshot (Core A; $t = 1.7 \times 10^4$ yr), shown in Fig. 6. A face-on intensity map of this object is shown in Fig. 1. First, we identify the principle axes of the
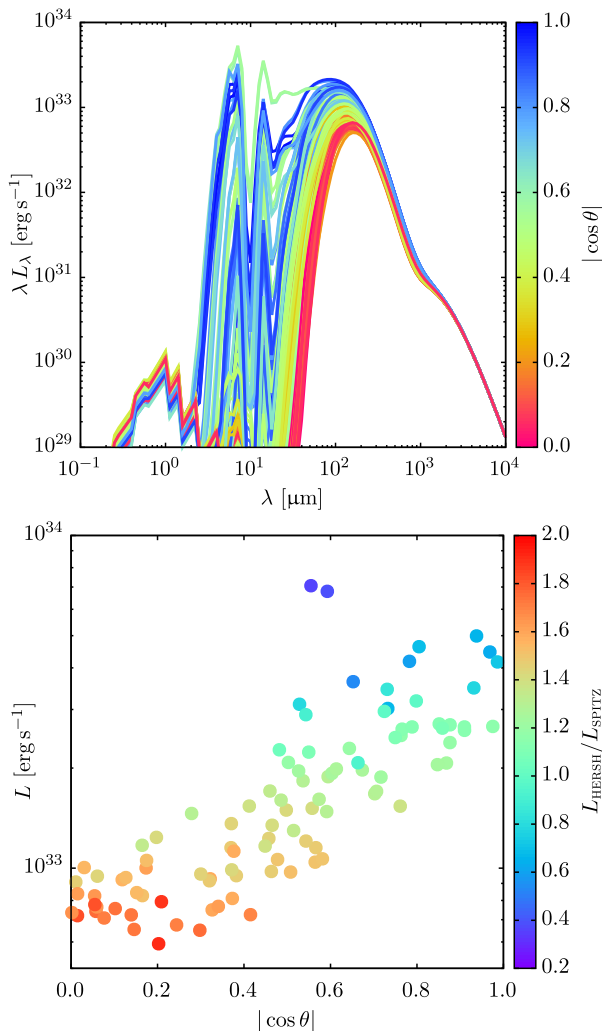
Figure 6. SEDs from Core A at $t = 1.7 \times 10^4$ yr. The top frame shows the full SED with the inclination angle θ indicated by the colour scale. Note, $|\cos\theta| = 1$ corresponds to an approximately face-on view, $\cos\theta = 0$ corresponds is an approximately edge-on view. The bottom frame shows the apparent luminosity as a function of inclination angle. Here, the colour scale shows the infrared colour, as defined in Fig. 5.

system by calculating the inertia tensor for the ensemble of SPH and sink particles. For a flatted rotating object (e.g. a disc), the eigenvector with the largest eigenvalue roughly corresponds to the rotation axis. We define the inclination angle θ as the angle between the this direction and SED viewing angle.

We show that, similar to single protostars, the apparent luminosity of the protostellar system is strongly correlated with the viewing angle. In this case, the luminosity when viewed face-on is up to an order of magnitude greater than that when viewed edge-on. There is some scatter in the luminosity–angle relationship, which is most likely due to (i) non-axisysmmetric variations in the plane of the system, and (ii) possible deviations between the principle axis and the *true* axis of rotation. We find that the colour of the system is also strongly correlated with the viewing angle. For observed objects where the apparent luminosity, colour and inclination angle are known, this provides a useful tool for estimating its average (or *true*) luminosity.

4.3 Comparison of radiative transfer methods

The SW07 radiative transfer approximation and the Monte Carlo approach used by SPAMCART differ considerably. We discuss these differences in detail in Appendix C. In summary, the SW07 method usually calculates temperatures similar to SPAMCART. The main exception is within the inner 70 au of protostellar discs. Here, the SW07 method calculates temperatures, which are roughly an order of magnitude greater than those from SPAMCART. Analytical and numerical calculations of disc fragmentation (e.g. Whitworth & Stamatellos 2006; Clarke 2009; Stamatellos & Whitworth 2009) strongly suggest that disc fragmentation should occur outside this radius. We further note that the high inner-disc temperatures can only suppress fragmentation in these regions. The hypothesis that most brown dwarfs and very low mass stars are formed via disc fragmentation (e.g. Lomax et al. 2014, 2015) is therefore *not* undermined by the inaccuracy of the temperature calculation in the SW07 method.

5 DISCUSSION

The SPH simulations here, along with other work (e.g. Lomax et al. 2014, 2015) challenge the notion that solar-type and low-mass stars have a simple evolutionary progression from prestellar cores to main-sequence stars. Under the conventional model, a prestellar core collapses to form a single class 0 protostar (e.g. Andre, Ward-Thompson & Barsony 2000). A circumstellar disc forms and material steadily accretes on to the protostar through the class I, class II, and class III phases, after which the star progresses on to the main sequence (e.g. Lada 1999). We suggest that, since cores are turbulent, they frequently fragment into multiple objects. Once this occurs, N-body processes and anisotropic accretion can produce protostellar multiple systems with separations, $s \gtrsim 1$ au, and highly varied morphologies. This makes interpreting observations difficult as there is a significant chance that one or more protostars will be in the same telescope beam. This is even true for powerful interferometers such as the Very Large Array (VLA) and the Atacama Large Millimetre Array (ALMA).

5.1 SED fitting methodology

It may be possible to use simulations to address difficulties in fitting model protostars to observations. For simplicity, we will discuss only protostellar SEDs. If we consider a protostellar system with

parameters $\boldsymbol{\theta}$ (e.g. number of objects, primary/secondary luminosity, primary/secondary disc mass, and circumstellar disc mass, etc.), the posterior probability of $\boldsymbol{\theta}$, given some observed data D, is given by Bayes' theorem,

$$P(\boldsymbol{\theta}|D) = \frac{P(D|\boldsymbol{\theta})\, P(\boldsymbol{\theta})}{P(D)}. \tag{7}$$

Here, $P(D|\boldsymbol{\theta})$ is the likelihood of D, given $\boldsymbol{\theta}$, $P(\boldsymbol{\theta})$ is the a priori probability of $\boldsymbol{\theta}$ and $P(D)$ is a normalization constant such that integral of $P(\boldsymbol{\theta}|D)$ over all $\boldsymbol{\theta}$ is equal to one. Two difficulties arise from this analysis. First, the number of dimensions in $\boldsymbol{\theta}$-space can be arbitrarily large. For example, Robitaille (2017) defines a single protostar using a parameter space with at least seven dimensions. This scales superlinearly with number of possible objects you permit in a multiple system, for example, a quadruple system under this model has at least 28 parameters. If the prior distribution is uninformative (usually uniform or log-uniform between upper and lower limits along each dimension), then the number of sampling points required to cover the parameter space increases geometrically with each additional object. Secondly, fits to protostellar SEDs are often degenerate. A notable example of this is the degeneracy between disc mass and temperature caused by the Rayleigh–Jeans tail of the *Planck* function.

Both of these issues can be addressed by performing a large number of core simulations, with initial conditions representative of star-forming regions (e.g. Lomax et al. 2014), and using the results as an informative prior. First, we run m simulations and take n snapshots from each. We post-process each snapshot p times from different random viewing directions. This produces $N = m\, n\, p$ synthetic observations, each with $\boldsymbol{\theta}_j$ which is measured from the snapshot. Here, $\boldsymbol{\theta}_j$ is effectively sampled from a prior probability distribution defined by the suite of simulations. A posterior probability distribution can be estimated by calculating χ^2 likelihoods for each $\boldsymbol{\theta}_j$, which, in turn, can be used to estimate parameter expectation values.

Performing an analysis using this method eliminates the need to explicitly set up an arbitrarily large parameter space with an associated prior distribution. Furthermore, the simulation parameters are hyperparameters (i.e. parameters of the prior distribution) of the posterior distribution. This helps to lift degeneracies in SED fits; when the likelihood is unable to discriminate between degenerate combinations of parameters, the posterior is determined by the simulations instead. However, the hyperparameters are likely to have an affect on the posterior. The simulations presented here have caveats and limitations (discussed in Section 5.2), which would inevitably affect this analysis. We therefore stress that this methodology must be repeated as the state of the art (e.g. sophistication of numerical models and available computing resources) progresses. Furthermore, statements from any Bayesian analysis are entirely dependent on the model used. We envisage that comparing the results of this analysis with multiple models would have one of two main outcomes. First, ideally, the results may vary little when different models are used. This allows us to confidently place constraints on the physical properties of protostars. Secondly, the results may deviate when different models are used. While this is less ideal than the first case, it still provides a means of quantitatively comparing the outcomes of different models, given observations. This may aid further research in eliminating or reconciling various models.

Such an analysis requires a much larger suite of simulations than that presented here. This is numerically feasible, given that each simulation *unit*, i.e. an SPH simulation plus 4×10^4 synthetic observations, requires $\sim 4 \times 10^4$ CPU hours on current hardware.

Scaling this up to, say, 100 units is easily achievable over a year with large computing clusters, for example, the Distributed Research utilizing Advanced Computing (DiRAC) supercomputing facilities.

5.2 Caveats

We have presented a sophisticated suite of numerical simulations, which follow the observational properties of protostellar multiple systems over time. However, there are some important caveats we must address.

The resolution of the SPH simulations matches the requirements of modelling the hydrodynamics and self gravity of star formation. These do not necessarily match the requirements of modelling full radiative transfer through the ISM. The method presented here conserves photons *exactly* during the temperature calculations. However, the ray-tracing method used to generate the synthetic observations is approximate. In regions with extreme temperature gradients (e.g. in the vicinity of sinks), lack of resolution can cause the ray-trace to overestimate the intensity (and hence luminosity) by 30–50 per cent.

The interstellar radiation field is assumed to be isotropic and unattenuated by the core's parent molecular cloud. It is therefore only a rough estimate of the external heating. In nature, the strength of this term varies from region to region. For deeply embedded starless cores, the radiation field is attenuated by dust. Conversely, starless cores near high-mass stars have a greater degree of heating. However, once a protostar forms, it quickly becomes the dominant heating source for the core. Here, effect of the background on integral quantities, such as luminosity and colour, is negligible.

We have not modelled jets in the SPH simulations. This means that there are no cavities in the core envelopes above and below the protostellar poles. As a result, there may be less mid-infrared energy in the face-on system SEDs than there should be. A sub-grid model of protostellar jets (P. Rohde and S. Walch, private communication) is in development for the GANDALF SPH code (Hubber, Rosotti & Booth 2018) and will be included in future studies.

We use a single dust model throughout the density field, which does not account for polycyclic aromatic hydrocarbons (PAHs) or large coagulated dust grains with icy mantles (e.g. Ossenkopf & Henning 1994). We also assume that the dust-to-gas mass ratio is fixed outside dust sublimation regions. Modelling the evolution and dynamics of dust is complicated (e.g. Hubber et al. 2018; Ragusa et al. 2017) and will need to be considered in future.

The SWH11 model assumes that a protostellar photosphere is a blackbody with a variable luminosity and a fixed radius. The luminosity is sensitive to the sub-grid accretion model, the parameters of which have weak observational constraints (see SWH11 and references therein). When applying these models to SED fitting, the luminosity should not be interpreted as a proxy for stellar mass or accretion rate.

6 SUMMARY

We have presented synthetic observations of three protostellar multiple systems at different points in time, viewed from different angles. The gas dynamics of the systems are modelled using SPH, and the synthetic observations are generated using the SPAMCART post-processing Monte Carlo radiative transfer code. These are the first synthetic observations of protostars, which take into account episodic accretion and multiplicity. We note that we have modified SPAMCART so that it now accounts for dust scattering and extremely optically thick objects, such as protostellar discs. The SPAMCART code

makes full use of the detailed SPH particle distribution and we are able to resolve spatial scales $r \lesssim 0.1$ au, which is equivalent to the dust sublimation radii of protostars.

There is a growing amount of observational and numerical evidence indicating that many stars begin their lives in multiple systems. This suggests that studies which attempt to infer the physical properties of observed protostars using single star models may be inappropriate. We propose a Bayesian methodology, based on an expansion of the calculations presented here, that can be used to infer the physical properties of potentially multiple protostellar systems. We plan to undertake this project in the near future.

ACKNOWLEDGEMENTS

REFERENCES

Andre P., Ward-Thompson D., Barsony M., 2000, Protostars and Planets IV, 59

André P., Belloche A., Motte F., Peretto N., 2007, A&A, 472, 519

Balbus S. A., Hawley J. F., 1991, ApJ, 376, 214

Bate M. R., 2009, MNRAS, 392, 1363

Bate M. R., 2014, MNRAS, 442, 285

Bell K. R., Lin D. N. C., 1994, ApJ, 427, 987

Bisbas T. G. et al., 2015, MNRAS, 453, 1324

Clarke C. J., 2009, MNRAS, 396, 1066

Gammie C. F., 2001, ApJ, 553, 174

Gordon K. D. et al., 2017, A&A, 603, A114

Greene T. P., Aspin C., Reipurth B., 2008, ApJ, 135, 1421

Harries T. J., 2011, MNRAS, 416, 1500

Hartmann L., Kenyon S. J., 1996, ARA&A, 34, 207

Holman K., Walch S. K., Goodwin S. P., Whitworth A. P., 2013, MNRAS, 432, 3534

Hubber D. A., Batty C. P., McLeod A., Whitworth A. P., 2011, A&A, 529, A27

Hubber D. A., Walch S., Whitworth A. P., 2013, MNRAS, 430, 3261

Hubber D. A., Rosotti G. P., Booth R. A., 2018, MNRAS, 473, 1603

Johnstone D., Hendricks B., Herczeg G. J., Bruderer S., 2013, ApJ, 765, 133

Kenyon S. J., Hartmann L. W., Strom K. M., Strom S. E., 1990, AJ, 99, 869

Kraus A. L., Ireland M. J., Martinache F., Hillenbrand L. A., 2011, ApJ, 731, 8

Krumholz M. R., 2006, ApJ, 641, L45

Krumholz M. R., Cunningham A. J., Klein R. I., McKee C. F., 2010, ApJ, 713, 1120

Lada C. J., 1999, in Lada C. J., Kylafis N. D., eds., NATO ASIC Proc. 540: The Origin of Stars and Planetary Systems. Springer, p. 143

Li A., Draine B. T., 2001, ApJ, 554, 778

Lomax O., Whitworth A. P., 2016, MNRAS, 461, 3542 (LW16)

Lomax O., Whitworth A. P., Hubber D. A., Stamatellos D., Walch S., 2014, MNRAS, 439, 3039

Lomax O., Whitworth A. P., Hubber D. A., 2015, MNRAS, 449, 662

Lomax O., Whitworth A. P., Hubber D. A., Stamatellos D., Walch S., 2015, MNRAS, 447, 1550

Lucy L. B., 1999, A&A, 344, 282

Min M., Dullemond C. P., Dominik C., de Koter A., Hovenier J. W., 2009, A&A, 497, 155

Morris J. P., Monaghan J. J., 1997, J. Comput. Phys., 136, 41

Offner S. S. R., Klein R. I., McKee C. F., Krumholz M. R., 2009, ApJ, 703, 131

Offner S. S. R., Kratter K. M., Matzner C. D., Krumholz M. R., Klein R. I., 2010, ApJ, 725, 1485

Ossenkopf V., Henning T., 1994, A&A, 291, 943

Peneva S. P., Semkov E. H., Munari U., Birkle K., 2010, A&A, 515, A24

Porter T. A., Moskalenko I. V., Strong A. W., Orlando E., Bouchet L., 2008, ApJ, 682, 400

Ragusa E., Dipierro G., Lodato G., Laibe G., Price D. J., 2017, MNRAS, 464, 1449

Reipurth B., 1989, Nature, 340, 42

Robitaille T. P., 2010, A&A, 520, A70

Robitaille T. P., 2017, A&A, 600, A11

Robitaille T. P., Whitney B. A., Indebetouw R., Wood K., Denzmore P., 2006, ApJ, 167, 256

Stamatellos D., Whitworth A. P., 2008, A&A, 480, 879

Stamatellos D., Whitworth A. P., 2009, MNRAS, 392, 413

Stamatellos D., Whitworth A. P., Bisbas T., Goodwin S., 2007, A&A, 475, 37 (SW07)

Stamatellos D., Whitworth A. P., Hubber D. A., 2011, ApJ, 730, 32 (SWH11)

Stamatellos D., Whitworth A. P., Hubber D. A., 2012, MNRAS, 427, 1182

Tobin J. J. et al., 2016, ApJ, 818, 73

Toomre A., 1964, ApJ, 139, 1217

Weingartner J. C., Draine B. T., 2001, ApJ, 548, 296

Whitworth A. P., Stamatellos D., 2006, A&A, 458, 817

Zhu Z., Hartmann L., Calvet N., Hernandez J., Muzerolle J., Tannirkulam A.-K., 2007, ApJ, 669, 483

Zhu Z., Hartmann L., Gammie C., 2009, ApJ, 694, 1045

Zhu Z., Hartmann L., Gammie C., 2010, ApJ, 713, 1143

Zhu Z., Hartmann L., Gammie C. F., Book L. G., Simon J. B., Engelhard E., 2010, ApJ, 713, 1134

APPENDIX A: NUMERICAL TREATMENT OF DUST RADIATIVE TRANSFER

A1 Dust properties

We use the values of κ_λ, σ_λ, and mean scattering cosine g_λ derived by (Li & Draine 2001). The dust is a mixture of carbonaceous and amorphous silicate grains, with a size distribution following Weingartner & Draine (2001) at $R_v = 5.5$, and a dust-to-gas mass ratio of one percent. We simplify the treatment of dust scattering by approximating the scattering phase function $p_\lambda(\cos\theta)$ with a linear combination of isotropic scattering and pure forward or backward scattering. Here,

$$p_\lambda(\cos\theta) = \begin{cases} \frac{1}{2}(1 - g_\lambda) + 2\,g_\lambda\,\delta(\cos\theta - 1), & g_\lambda > 0; \\ \frac{1}{2}(1 + g_\lambda) - 2\,g_\lambda\,\delta(\cos\theta + 1), & g_\lambda < 0; \\ \frac{1}{2}, & g_\lambda = 0, \end{cases} \quad \text{(A1)}$$

where $-1 \leq \cos\theta \leq 1$. This phase function can be implemented in a numerical code when we note that the delta function component represents a modification to the local scattering mean free path l_λ, i.e.

$$l'_\lambda = \sum_{n=0}^{\infty} l_\lambda\,g_\lambda^n = \frac{l_\lambda}{1 - g_\lambda}. \quad \text{(A2)}$$

We may therefore model scattering as a completely isotropic process by defining a replacement set of optical properties:

$$\sigma'_\lambda \equiv (1 - g_\lambda)\sigma_\lambda;$$
$$\kappa'_\lambda \equiv \kappa_\lambda;$$
$$g'_\lambda \equiv 0. \quad \text{(A3)}$$

A2 Dust sublimation

We assume that dust sublimation occurs at temperatures above $T_{SUB} = 1000$ K. We reduce the dust-to-gas mass ratio for each particle by a factor a_i, which is calculated from N_{NEIB} neighbours,

$$a_i = \sum_{j=1}^{N_{NEIB}} \frac{m_j}{h_i^3 \rho_i} w(r_{ij}) \max[H(T_{SUB} - T_j), \epsilon]. \qquad (A4)$$

Here, h is the particle smoothing length, ρ is the particle density, $w(r)$ is the smoothing kernel function, $H(T)$ is the Heaviside step function, and ϵ is the smallest floating point number where $1 + \epsilon > 1$ ($\epsilon \simeq 2 \times 10^{-16}$ for 64 bit floating point variables). This ensures that $a_i \cong 1$ if $T_j < T_{SUB}$ is true for all neighbouring particles and $a_i \cong \epsilon$ if $T_j \geq T_{SUB}$ for all neighbours.

A3 Modified random walk

In very optically thick regions, such as the mid-planes of discs, the mean free path of the luminosity packets may be several orders of magnitude smaller than the local particle smoothing length. In these situations, following the full trajectory of the packet is prohibitively expensive. We address this by using the modified random walk (MRW) algorithm, originally presented by Min et al. (2009) and simplified by Robitaille (2010).

In its original form, the MRW moves packets through grid cells, which have uniform Planck inverse mean volume opacity, $\bar{\chi}_{VOL} = \rho \bar{\chi}_{INV}(T)$, where

$$\bar{\chi}_{INV}(T) = \frac{\int_0^\infty B_\lambda(T) \, d\lambda}{\int_0^\infty \chi_\lambda^{-1} B_\lambda(T) \, d\lambda}. \qquad (A5)$$

Here, a packet, which has diffused to some distance r_{MRW} from its origin r_0, has a total random walk length

$$s_{RW} = -\ln y \left(\frac{r_{MRW}}{\pi}\right)^2 3 \bar{\chi}_{VOL}, \qquad (A6)$$

where y is found by numerically inverting the equation,

$$\mathcal{R} = 2 \sum_{n=1}^\infty (-1)^{n+1} y^{n^2}, \qquad (A7)$$

and $\mathcal{R}$ is randomly drawn from the uniform distribution in the interval [0, 1]. In practice, a packet is moved a distance r_{MRW} (within the same cell) from r_0 to r_1 with a random isotropic direction $\hat{r}$. The distance s_{RW} is used instead of r_{MRW} to update the energy absorption rate. In order to apply this method here, we must (i) formulate a column density equivalent of equation A6 and (ii) and account for inhomogeneity of $\bar{\chi}_{VOL}(r)$ within a smoothed particle ensemble.

During a MRW step, a packet moves some number of mean free paths τ_{MRW}. The relationship between τ_{MRW} and distance r_{MRW} is defined as

$$\tau_{MRW} = \int_C \bar{\chi}_{VOL}(r) \, ds, \qquad (A8)$$

where C is the line segment,

$$r = r_0 + s \hat{r}, \quad 0 \leq s \leq r_{MRW}. \qquad (A9)$$

Here, a solution for r_{MRW} given τ_{MRW} is found using the modified Newton–Raphson method detailed by LW16.

We perform a MRW step from r_0 to r_1 if the local mean free path $\bar{\chi}_{VOL}^{-1}(r_0)$ is a factor of a few less than the local smoothing length

$h(r_0)$. Our choice of τ_{MRW} depends on the local environment:

$$\tau_{MRW} = \min\left(h(r_0) \bar{\chi}_{VOL}(r_0), \frac{\bar{\chi}_{VOL}(r_0)^2}{2\|\nabla \bar{\chi}_{VOL}(r_0)\|}\right). \qquad (A10)$$

The first term on the right-hand side ensures that $r_{MRW} \lesssim h(r_0)$; the second terms attempts to keep r_{MRW} finite for all values of $\hat{r}$. The quantities $h(r_0)$, $\bar{\chi}_{VOL}(r_0)$, and $\nabla \bar{\chi}_{VOL}(r_0)$ are estimated using SPH scatter calculations. We pick a random $\hat{r}$, calculate r_{MRW}, and move the packet to position $r_1 = r_0 + r_{MRW} \hat{r}$. The energy absorption and scattering rates of particles intersected by the path (see equation 1 and 2) are updated,

$$\dot{A}_i \rightarrow \dot{A}_i + \mathcal{W}_i \left(\frac{s_{RW}}{r_{MRW}}\right) \frac{\ell_j}{m_i} \kappa_P(T_i) \varsigma_{ij},$$

$$\dot{S}_{i\lambda} \, d\lambda \rightarrow \dot{S}_{i\lambda} \, d\lambda + \mathcal{W}_i \left(\frac{s_{RW}}{r_{MRW}}\right) \frac{\ell_j}{m_i} \sigma_P(T_i, \lambda, d\lambda) \varsigma_{ij}. \qquad (A11)$$

Here, $\sigma_P(T, \lambda, d\lambda)$ is the partial Planck mean mass scattering coefficient,

$$\sigma_P(T, \lambda, d\lambda) = \frac{\int_\lambda^{\lambda+d\lambda} \sigma_{\lambda'} B_{\lambda'}(T) \, d\lambda'}{\int_0^\infty B_{\lambda'}(T) \, d\lambda'}. \qquad (A12)$$

The expression (s_{RW}/r_{MRW}) is found by rearranging equation A6 and replacing $r_{MRW} \bar{\chi}_{VOL}$ with τ_{MRW} from equation A8, i.e.

$$\left(\frac{s_{RW}}{r_{MRW}}\right) = -\ln y \, \frac{3 \tau_{MRW}}{\pi^2}. \qquad (A13)$$

We include a weighting term $\mathcal{W}_i$ which takes into account the variation in volume opacity along the random walk. Here,

$$\mathcal{W}_i = \rho_i \, \bar{\chi}_{INV}(T_i) \frac{\sum_k \bar{\chi}_P(T_k) \varsigma_{kj}}{\sum_k \rho_k \, \bar{\chi}_{INV}(T_k) \, \bar{\chi}_P(T_k) \varsigma_{kj}}, \qquad (A14)$$

where k are the indices of all intersected particles and $\chi_P(T)$ is the Planck mean mass opacity coefficient. This term makes sure that the share of s_{RW} assigned to each particle is proportional to the volume opacity of each particle. In regions with roughly homogeneous volume opacity, $\mathcal{W}_i$ is approximately equal to one.

APPENDIX B: KIRCHOFF'S LAW BENCHMARK

An object in radiative equilibrium with a uniform blackbody background radiation field, $I_{\lambda BG} = B_\lambda(T_{BG})$, should have temperature T_{BG}. This becomes apparent by stating that the energy absorption rate at on the surface of the object $\mathcal{A}$ equal to the emission rate $\mathcal{E}$, where

$$\mathcal{A} = \pi \int_A \int_{\lambda=0}^\infty I_{\lambda BG} \alpha_\lambda \, d\lambda \, dA \,;$$

$$\mathcal{E} = \pi \int_A \int_{\lambda=0}^\infty B_\lambda(T_{OB}) \epsilon_\lambda \, d\lambda \, dA. \qquad (B1)$$

Here, α_λ and ϵ_λ are the absorptivity and emissivity, respectively, and T_{OB} is the surface temperature of the object. Kirchoff's law of thermal radiation states $\alpha_\lambda = \epsilon_\lambda$. If $I_{\lambda BG} = B_\lambda(T_{BG})$, then T_{OB} must equal T_{BG} in order to satisfy the condition $\mathcal{A} = \mathcal{E}$. Furthermore, the intensity at the object's surface $I_{\lambda OB}$ is equal to $I_{\lambda BG}$ and the object
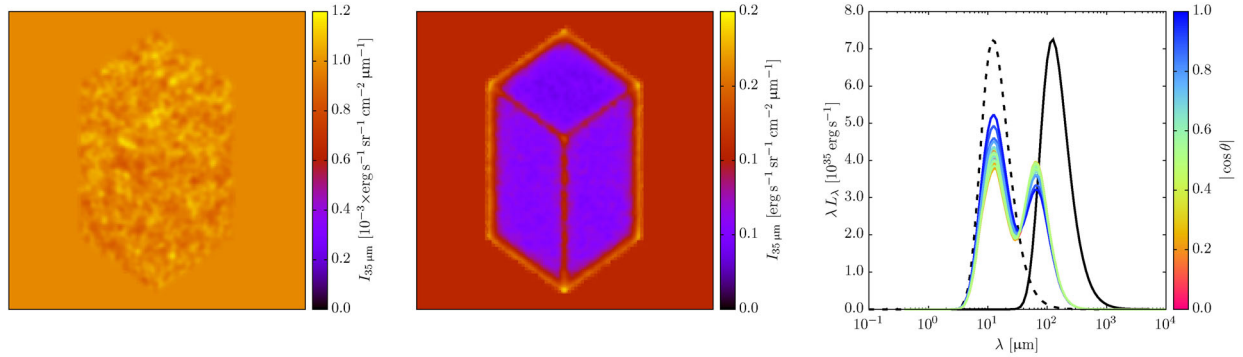
Figure B1. The left-hand panel and centre frames show the 35 μm intensity maps of the cuboid in Field A (left-hand panel) and Field B (centre panel), offset from its principle axes by $45°$. The edge-length of both frames is 1300 au. The right frame shows the SED of the cuboid in Field A (black solid lines) and Field B (multicoloured lines) along with a 300 K blackbody SED diluted by a factor of 10^{-4}. The colour scale shows the angle between the long axis of the cuboid and the direction normal to the viewing plane. When the cuboid is viewed along the long axis, $|\cos\theta| = 1$; when the long axis is parallel to the plane of the sky, $\cos\theta = 0$. Note that the solid black line is actually 30 overlaid SEDs, which are indistinguishable on this plot.

is indistinguishable from the background. Note that in this example we have omitted the directional dependence from the terms to simplify the equations; the above still holds if directional dependence is included. If we dilute the background radiation field, i.e. $I_{\lambda\text{BG}} = d\, B_\lambda(T_{\text{BG}})$, where $d < 1$, then $T_{\text{OB}} < T_{\text{BG}}$. This will result in short-wavelength radiation being absorbed and reemitted at longer wavelengths. The effect of this on the SED of an object is difficult to predict quantitatively without numerical calculations, however we should see a reduction in the background SED and a second peak at a longer wavelengths than the background.

We re-examine the test of Kirchoff's law presented by LW16. The original test demonstrated that SPAMCART adheres to Kirchoff's law when a spherically symmetric distribution of particles is irradiated. Here, we perform a similar test, but with a non-spherically symmetric distribution of particles. We construct a cuboid of 2×10^5 SPH particles, with total mass $2\,\text{M}_\odot$ and dimensions $2000 \times 1000 \times 1000$ au. This is illuminated by two background fields: Field A, which has the SED of an undiluted 30 K blackbody; and Field B with has the SED of a 300 K blackbody, diluted by a factor of 10^{-4}. In each case, the field is simulated using 10^6 luminosity packets and five iterations. The SEDs and intensity maps are constructed for 30 random viewing angles.

Fig. B1 shows example intensity maps and the SEDs of the illuminated cuboids. The two maps show the intensity at 35 μm. With Field A, the surface of the cuboid has the same intensity as the background, modulo fluctuations of about 20 per cent. At these wavelengths, the path through the cuboid corresponds to 30–60 optical depths. Most of the emission associated with the cuboid is generated from the outermost layer of SPH particles only. At wavelengths closer to the peak emission – say, 200 μm – the intensity fluctuations relative to the blackbody background are $\ll$1 per cent. The SEDs for all 30 viewing angles are indistinguishable from a 30 K blackbody. With Field B, the cuboid casts a silhouette over the background at 35 μm. The edges of the cuboid are warmer than the faces (the corners warmer still) because they are heated from multiple directions. The SEDs show that the cuboid reduces the flux arriving from the background radiation field. This is most pronounced when the long axis of the cuboid is parallel to the image plane. The absorbed emission is reemitted by the cuboid at $\sim$70 μm, where it is noticeably brighter than the background. In summary, the numerical results from SPAMCART are in agreement with our predictions based on Kirchoff's law.
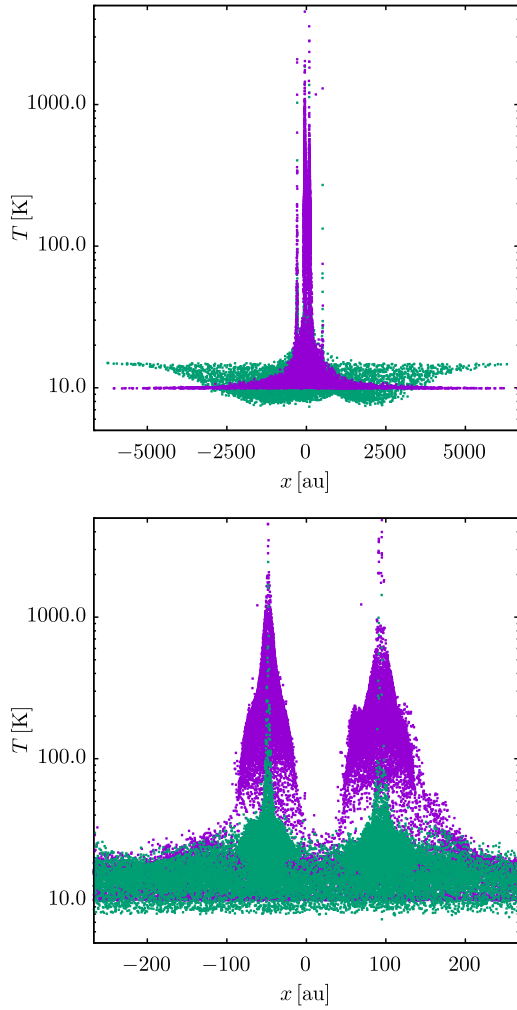
APPENDIX C: COMPARISON OF RADIATIVE TRANSFER METHODS

The Monte Carlo radiative transfer calculations presented here differ significantly from the SW07 radiative transfer approximation used in the SPH simulations. Here, we provide a brief discussion of these differences. The SW07 method approximates radiative cooling and heading rates by assuming that each particle is embedded in a polytropic pseudo-cloud. The physical properties of the pseudo-cloud are tuned to the density, temperature, and gravitational potential at the particle position. This is used to calculate a mass-weighted exit optical depth from the pseudo-cloud, which is, in turn, used to estimate the amount of radiative shielding affecting the heating and cooling rate of each particle. Table C1 gives a brief comparison of the physical assumptions used in SPAMCART and the SW07 method.

Fig. C1 shows the distribution of particle temperatures from a snapshot of Core A. Here, we have plotted temperatures calculated using SPAMCART and using the SW07 method. We note a number of differences in the temperatures. First, for the material within 70 au of sinks (i.e. accretion discs), the SW07 temperatures can be roughly an order of magnitude greater than the SPAMCART temperatures. This is because the SW07 method assumes spherical symmetry and therefore material cannot cool as efficiently as it physically should in the

Table C1. A brief summary of the physical assumptions used in the SPAMCART code compared with those used in the SW07 method.

	SPAMCART	SW07
Time dependence.	Equilibrium calculation.	Assumes thermalization time-scale.
Geometric assumptions.	None.	Spherical symmetry.
Heating sources.	Radiation from stars and background radiation field, scattered and absorbed/reemitted by dust.	Background temperature. Quartic sum of interstellar backgound ($T = 10\,\text{K}$) and local stellar temperature ($T \propto r^{-2}$). Heating from $P\,\text{d}V$ work done.
Opacity sources.	Dust (Li & Draine 2001; Weingartner & Draine 2001).	Dust and gas (Bell & Lin 1994).

presence of strong density gradients. Secondly, the distribution of temperatures in the inner core envelope ($R \lesssim 3000$ au) is more varied in the SPAMCART calculations than SW07. This is due to SPAMCART fully modelling anisotropies in the local radiation field (plus a small level of statistical noise). Finally, The SPAMCART temperature at the core boundary is a roughly 15 K, whereas the SW07 temperature is 10 K. This is due to differences in the Porter et al. (2008) radiation field used in SPAMCART and the assumed 10 K radiation field used by SW07.

Figure C1. Temperature versus x-coordinate for Core A at $t = 1.7 \times 10^4$ yr. The purple points show the temperatures calculated during the SPH simulations using the SW07 method. The green points show the temperatures calculated using SPAMCART. The two frames show the distribution at two different spatial scales.

This paper has been typeset from a TEX/LATEX file prepared by the author.